Electronic Supplementary Material (ESI) for Journal of Materials Chemistry A.

Supporting Information

Mechanically stable structured porous boron nitride with high volumetric adsorption capacity

*Tian Tian,[1] Jingwei Hou,[2] Humera Ansari,[3] Ying Xiong,[1] Anouk L'Hermitte,[1,4] David Danaci,[1] Ronny Pini[3] and Camille Petit[1]**

[1] Barrer Centre, Department of Chemical Engineering, Imperial College London, South Kensington Campus, London SW7 2AZ, UK

[2] School of Chemical Engineering, University of Queensland, QLD, 4072, Australia

[3] Department of Chemical Engineering, Imperial College London, South Kensington Campus, London SW7 2AZ, UK

[4] Department of Materials, Imperial College London, South Kensington Campus, London SW7 2AZ, UK

* Corresponding author: camille.petit@imperial.ac.uk

1. Synthesis of structured BN

1.1. Effect of DCD on MF resin morphology

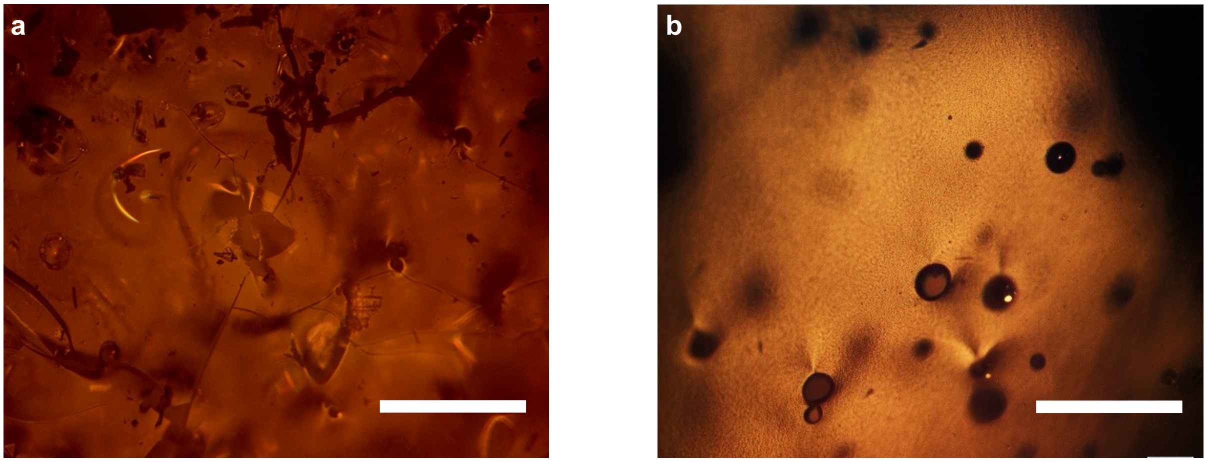

Figure S1. Microscope images of MF resin with (a) 0.5 g dicyandiamide and (b) 1.5 g DCD.

Scale bar = 100 µm.

Figure S2. Optical images of MF resin with 1.5 g dicyandiamide before the transparent samples were collected.

1.2. Effect of reaction gas on structured BN

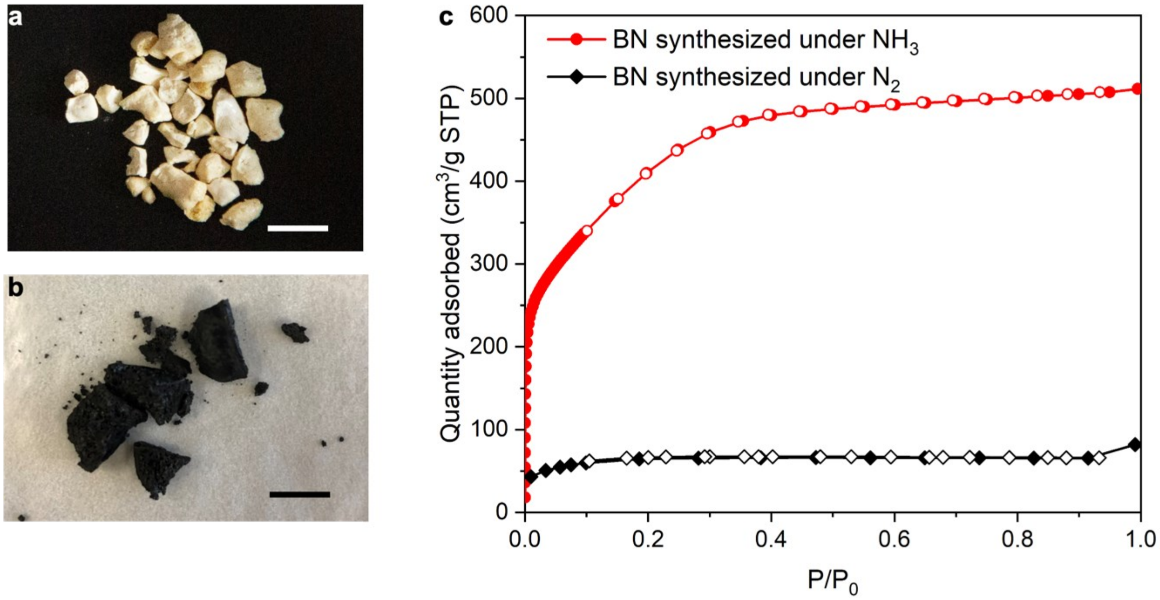

Figure S3. Optical images of porous BN obtained under (a) NH_3 and (b) N_2. Scale bar = 1 cm. c) N_2 sorption isotherms at 77 K for BN synthesized under NH_3 (red circles) and N_2 (black diamonds).

2. *Moisture stability of structured BN and powder BN*

The hydrolytic instability of porous BN has been highlighted in previous studies and represents a major barrier to industrial applications.[1,2] Figures S4 and S5 show the influence of moisture (> 99% humidity) exposure time on the BET area of structured BN and powder BN. Both samples show virtually the same BET areas after the first hour. However, the porosity decreased significantly after 2 h of exposure for powder BN, showing a 54% loss in the surface area. For structured BN, the reduction was of 18%. More importantly, structured BN maintains more than 60% of its original surface area after 8 h exposure, whereas powder BN only retains 15%. A 25% more drop of the surface area is observed for structured BN after further 4 h exposure, at which point powder BN is virtually non-porous.

We analysed structural changes in both samples upon exposure to moisture using XRD. In the case of powder BN (Figure S4b), the (002) peak related to hexagonal BN increases in intensity and shifts to higher angles after exposure to moisture. This observation agrees with previous studies and indicates a loss of the amorphous portion of BN upon decomposition in water, leaving the residual material with a higher crystallinity (i.e. lower porosity and surface area).[3] Structured BN exhibits a different trend (Figure S4c). The sample does not show any increase in crystallinity before 12 h of exposure. This observation suggests a slower degradation compared to powder BN, consistent with the BET area trend (Figure 5a). We attribute the greater hydrolytic stability of structured BN compared to that of powder BN to its lower content of oxygen atom (3 at% *vs* 9 at%). Indeed, oxygen sites are susceptible to hydrolysis attack as observed in other studies.[2]

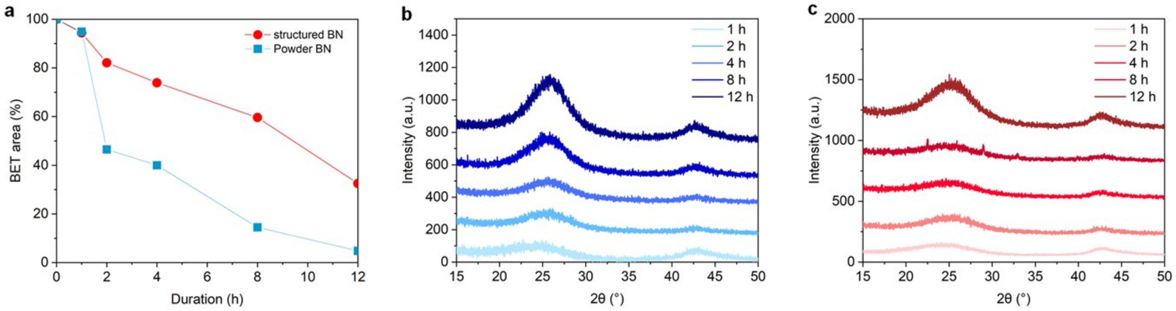

Figure S4. Structural features of structured BN and powder BN after moisture exposure. (a) BET surface area loss as derived from N_2 sorption at 77 K; (b) XRD patterns of powder BN; (c) XRD patterns of structured BN.

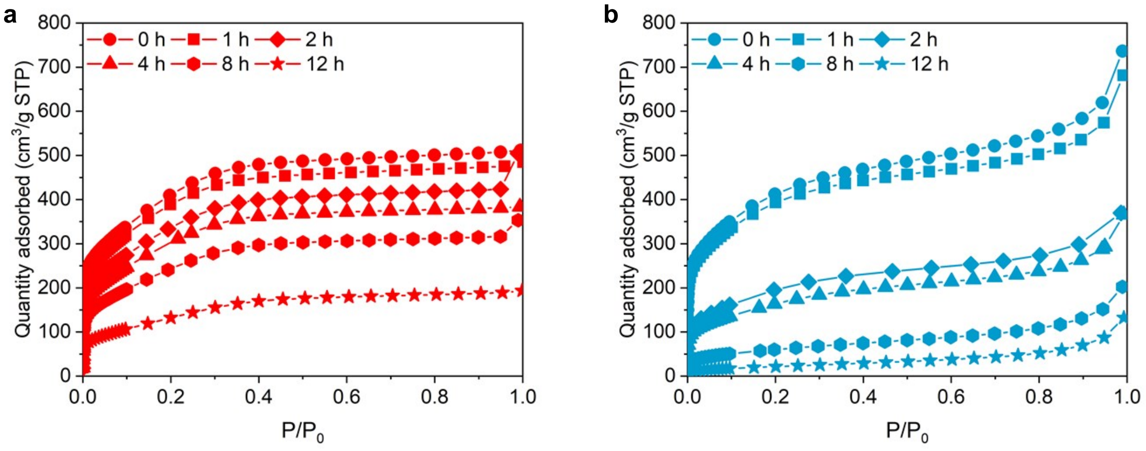

Figure S5. N_2 adsorption isotherms at 77 K after moisture exposure: (a) structured BN; (b) powder BN; 0 h, circle; 1 h, square; 2 h, diamond; 4 h, triangle; 8 h, hexagon; 12 h, star.

3. Electron microscope images of structured BN vs powder BN

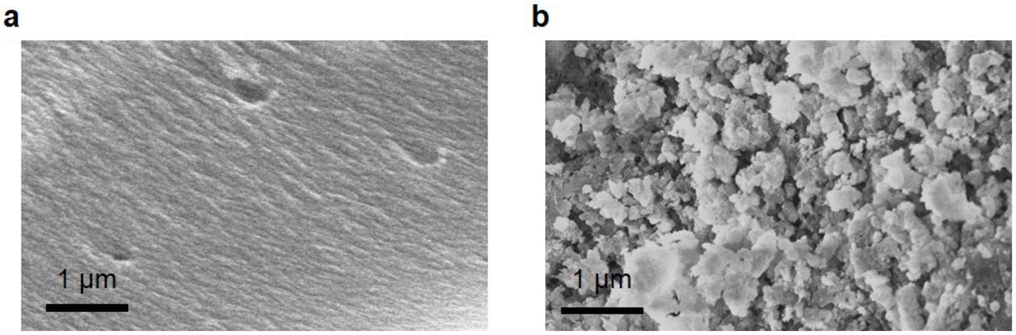

Figure S6. SEM images for a) structured BN; b) powder BN.

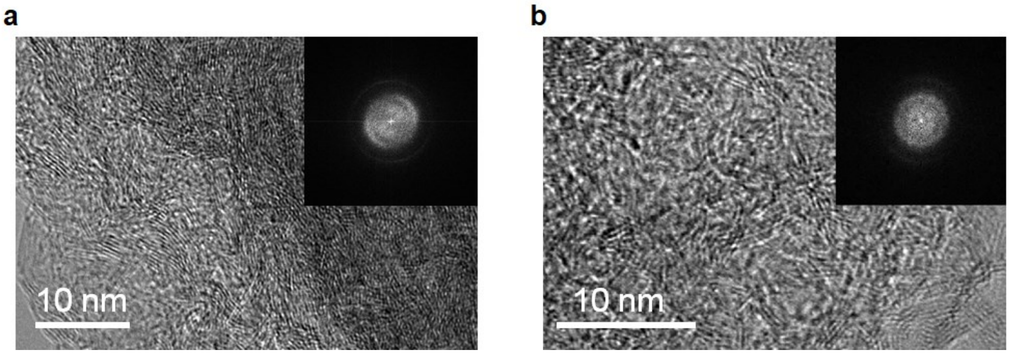

Figure S7. TEM images for a) structured BN; b) powder BN.

4. *Gas adsorption: structured BN vs powder BN*

4.1. N_2 adsorption isotherms at 77K.

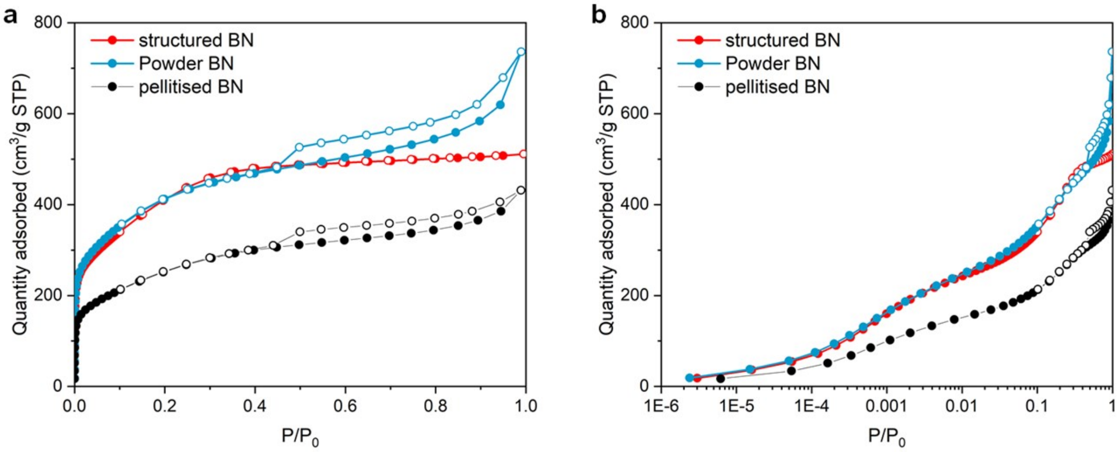

Figure S8. N_2 adsorption isotherms at 77 K for structured BN, powder BN and pelletised BN in a) linear scale; b) semi-logarithmic scale.

Table S1. Gravimetric surface area, bulk density, and volumetric surface area for selected high-surface-area BN.

Materials	S_{BET} (mass) [$m^2\ g^{-1}$]	ρ [$g\ cm^{-3}$]	S_{BET} (vol) [$m^2\ cm^{-3}$]	Reference
Structured BN	1523	0.31	473	This work
Powder BN	1500	0.21	315	This work
Pelletised BN	905	0.43	389	This work
Sintered BN	428	0.786	336	Bernard et al.[4]
BN foam	1406	0.18	253	Xue et al.[5]
BN foam	773	0.015	11.6	Lin et al.[6]
hBN aerogel	1080	1×10^{-4}	0.11	Xu et al.[7]
BN aerogel	920	0.015	13.8	Li et al.[8]

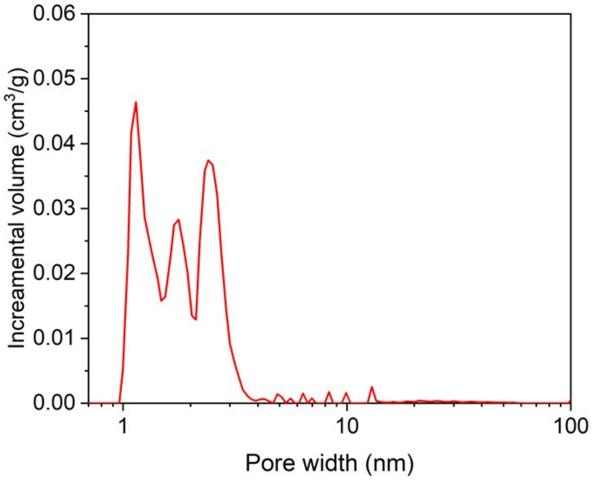

Figure S9. Pore size distribution of structured BN as derived from N_2 adsorption isotherms at 77 K.

4.2. Bulk density measurement via mercury porosimetry.

We measured the bulk density of both structured BN and powder BN using mercury porosimetry, a well-established technique that has been used to measure the bulk density of other porous materials. Mercury is a non-wetting liquid that does not intrude into small pores at ambient pressure, facilitating the measurement of bulk volume, which includes both the material volume and the interstitial volume, and thus the bulk density.

In a typical mercury intrusion porosimetry measurement, the sample is filled in a penetrometer, which has a known weight and volume. It should be noted that the sample is not mechanically compressed. After evacuation, the penetrometer is filled with mercury. The mercury will surround the sample at ambient pressure but not enter pores and voids smaller than ca. 6 μm. The weight of mercury is obtained by reweighing the penetrometer and by subtracting the known weights of the empty penetrometer and the sample. The volume of intruded mercury is then computed from the known mercury density (13.5394 g/mL) and the bulk volume of the sample is obtained as the difference between the empty penetrometer volume and the intruded mercury volume.

As powder BN and structured BN has the same composition and similar surface area, the materials volume of both samples can be exactly same. However, due to the more packed structure of structured BN (i.e. less interparticle volume), the structured BN shows much higher bulk density compared to powder BN.

4.3. Methane adsorption isotherms at 298 K.

The data of high-pressure methane uptake was obtained as excess gravimetric adsorption capacity (N_{exc}), and was converted into absolute gravimetric capacity (N_{abs}) using equation (1):

$$N_{abs} = N_{exc} + \rho_{gas} V_{micro} \quad (1)$$

where ρ_{gas} is the density of the non-adsorbed gas and V_{micro} is the micropore volume of the adsorbent. The skeleton volumes (0.474 cm^3/g for powder BN and 0.476 cm^3/g for structured BN) obtained by helium gravimetry were used to calculate the excess adsorbed capacity.[9]

Absolute volumetric adsorption capacity is converted from the absolute gravimetric uptake by multiplying by the *bulk density*. Bulk density is the ratio of the mass of an uncompressed solid sample and its volume, including the volume of the solid and the interparticle space.

Based on the strength of adsorption displayed by the isotherms, the adsorption of CH_4 on BN is expected to be based on physisorption.

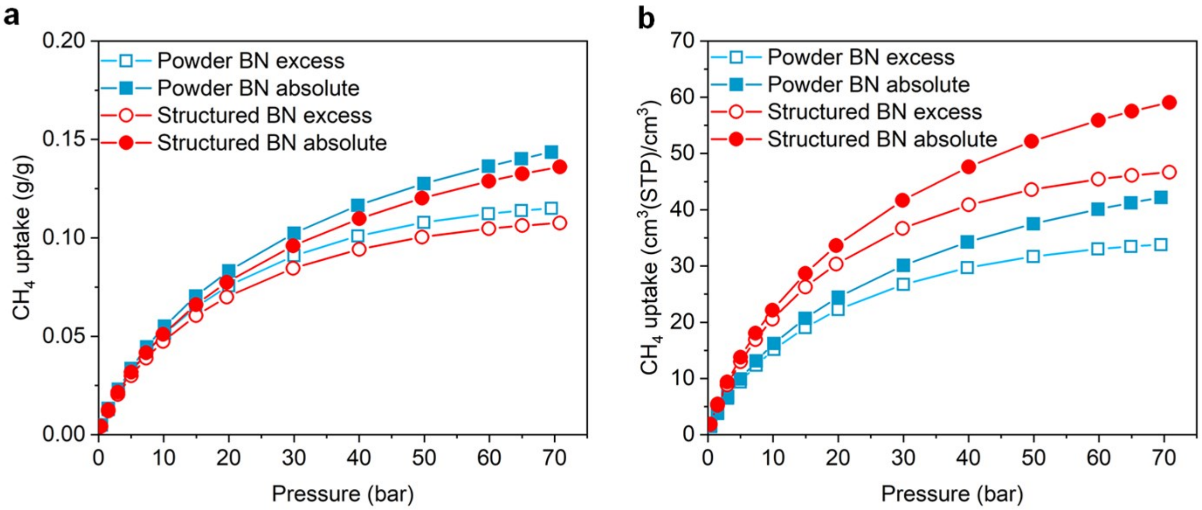

Figure S10. Comparison of absolute methane uptake at 298 K between powder BN (blue squares) and structured BN (red circles): a) gravimetric uptake; b) volumetric uptake.

Table S2. Surface area, methane storage capacity at RT and 65 (35) bar for selected porous materials at 298 K.

Materials	BET surface area $[m^2\ g^{-1}]$	Absolute uptake g/g	cm^3/cm^3	Reference
CC3β porous organic cage	652	0.064	28	Charles et al.[10]
5A	-	(0.05)	-	Rolniak et al.[11]
13X	-	(0.053)	-	Rolniak et al.[11]
MCM-41	1070	(0.065)	32	Menon et al.[12]
Saran A carbon monolith	1000	0.098	-	Menon et al.[12]
COF-5	1670	0.115	-	Furukawa and Yaghi[13]
Structured BN	1500	0.136	59	This work
NiMOF-74	1350	0.148	-	Peng et al.[14]
HKUST-1	1193	0.177	259	Tian et al.[15]
COF-102	3620	0.238	-	Furukawa and Yaghi[13]
LMA-738 carbon	3290	0.296	220	Casco et al.[16]

4.4. N_2 adsorption kinetics at 77 K

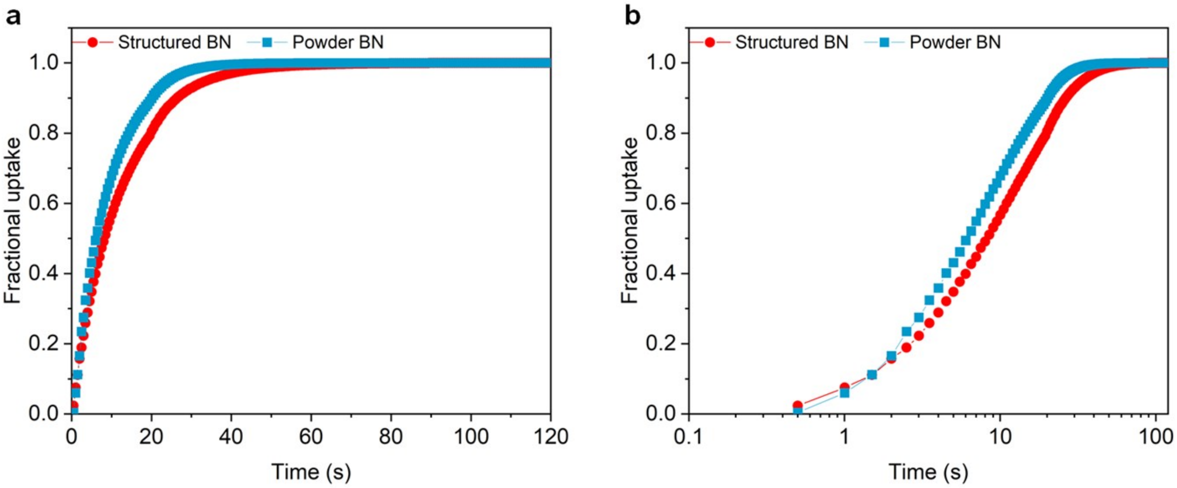

Figure S11. Comparison of adsorption kinetics of N_2 uptake at 77K and 2.2×10^{-6} bar between powder BN (blue) and structured BN (red circles): (a) linear scale, (b) log scale.

Fractional uptake based on Equation 2 is used to study the adsorption kinetics:

$$Fractional\ uptake = \frac{m_t - m_o}{m_{eq} - m_0} \tag{2}$$

where m_t is the adsorption amount at time t, m_0 is the adsorption amount at t = 0, and m_{eq} is the adsorption amount at equilibrium.

5. *Mechanical stability of structured BN*

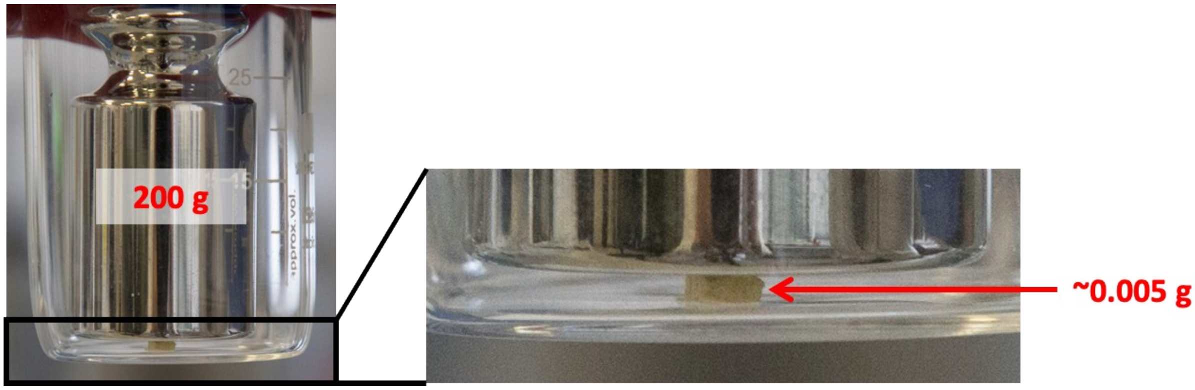

Figure S12. Optical image of structured BN under a 200 g calibration weight.

The mechanical stability is evaluated by Vickers microhardness test. To convert the Vickers hardness to SI unit (e.g. MPa), the value is multiplied by 9.807.[17]

6. Formation mechanism

FTIR was used to analyse the chemical composition of the intermediates. Sample collected at 200 °C shows NH_2 stretching band (3350 cm^{-1}), C-N stretching band (1560, 1450, 1320 cm^{-1}) and a triazine ring bending band (807 cm^{-1}).[18] All these bands indicate the successful synthesis of the MF resin. Because of the high mechanical strength of MF resin, which can be broken into small glassy pieces, together with the low content of B, the band attributed to B-containing bonds was not observed. Increasing the temperature to 300 °C leads to a new C-O stretching band at 1320 cm^{-1}. Both intermediates collected at 300 and 400 °C present an unknown band at around 880-890 cm^{-1}. This band is always present in melon-based materials, indicating the existence of melon-based polymer.[18] A new B-O stretching band (1390 cm^{-1}) is observed at 400 °C due to the increased percentage of B in the mixture.[19–22] A very broad band between 800-1700 cm^{-1} at 600 °C indicates the phase transition process at this temperature. Three main characteristic bands (~1360, 1100, 790 cm^{-1}) belonging to BN appear when the temperature increased to 800 °C clearly suggested the formation of BN. The IR features remained unchanged when the temperature increased to 1000 °C. The FTIR analysis supports the formation mechanism hypothesis concluded from XPS analysis.

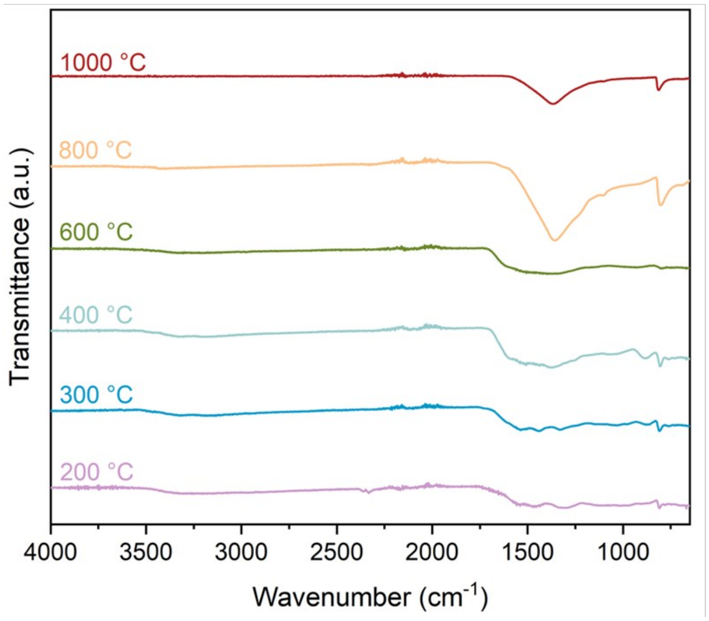

Figure S13. FTIR of intermediates obtained at different temperatures.

References

1 C. G. Cofer and J. Economy, *Carbon N. Y.*, 1995, **33**, 389–395.

2 R. Shankar, S. Marchesini and C. Petit, *J. Phys. Chem. C*, 2019, **123**, 4282–4290.

3 W. Lei, V. N. Mochalin, D. Liu, S. Qin, Y. Gogotsi and Y. Chen, *Nat. Commun.*, 2015, **6**, 1–8.

4 S. Bernard and P. Miele, *New J. Chem.*, 2014, **38**, 1923–1931.

5 Y. Xue, P. Dai, X. Jiang, X. Wang, C. Zhang, D. Tang, Q. Weng, X. Wang, A. Pakdel, C. Tang, Y. Bando and D. Golberg, *J. Mater. Chem. A*, 2015, **4**, 1469–1478.

6 J. Lin, X. Yuan, G. Li, Y. Huang, W. Wang, X. He, C. Yu, Y. Fang, Z. Liu and C. Tang, *ACS Appl. Mater. Interfaces*, 2017, **9**, 44732–44739.

7 X. Xu, Q. Zhang, M. Hao, Y. Hu, Z. Lin, L. Peng, T. Wang, X. Ren, C. Wang, Z. Zhao, C. Wan, H. Fei, L. Wang, J. Zhu, H. Sun, W. Chen, T. Du, B. Deng, G. J. Cheng, I. Shakir, C. Dames, T. S. Fisher, X. Zhang, H. Li, Y. Huang and X. Duan, *Science (80-.).*, 2019, **363**, 723–727.

8 G. Li, M. Zhu, W. Gong, R. Du, A. Eychmüller, T. Li, W. Lv and X. Zhang, *Adv. Funct. Mater.*, 2019, **29**, 1–7.

9 H. Ansari, L. Joss, J. Hwang, J. P. M. Trusler, G. Maitland and R. Pini, *Microporous Mesoporous Mater.*, 2020, **308**, 110537.

10 C. D. Charles and E. D. Bloch, *Supramol. Chem.*, 2019, **31**, 508–513.

11 P. D. Rolniak and R. Kobayashi, *AIChE J.*, 1980, **26**, 616–625.

12 V. C. Menon and S. Komarneni, *J. Porous Mater.*, 1998, **5**, 43–58.

13 H. Furukawa and O. M. Yaghi, *J. Am. Chem. Soc.*, 2009, **131**, 8875–8883.

14 Y. Peng, V. Krungleviciute, I. Eryazici, J. T. Hupp, O. K. Farha and T. Yildirim, *J. Am. Chem. Soc.*, 2013, **135**, 11887–11894.

15 T. Tian, Z. Zeng, D. Vulpe, M. E. Casco, G. Divitini, P. A. Midgley, J. Silvestre-Albero, J. C. Tan, P. Z. Moghadam and D. Fairen-Jimenez, *Nat. Mater.*, 2018, **17**, 174–179.

16 M. E. Casco, M. Martínez-Escandell, E. Gadea-Ramos, K. Kaneko, J. Silvestre-Albero and F. Rodríguez-Reinoso, *Chem. Mater.*, 2015, **27**, 959–964.

17 M. M. Yovanovich, *Collect. Tech. Pap. - 44th AIAA Aerosp. Sci. Meet.*, 2006, **16**, 11702–11729.

18 X. Wei, Y. Qiu, W. Duan and Z. Liu, *RSC Adv.*, 2015, **5**, 26675–26679.

19 C. Wu, B. Wang, N. Wu, C. Han, X. Zhang, S. Shen, Q. Tian, C. Qin, P. Li and Y. Wang, *Ceram. Int.*, 2020, **46**, 1083–1090.

20 X. Qiao, Z. Zhou, X. Liu, C. Zhao, Q. Guan and W. Li, *Catal. Sci. Technol.*, 2019, **9**, 3753–3762.

21 J. Xu, Y. Li, S. Peng, G. Lu and S. Li, *Phys. Chem. Chem. Phys.*, 2013, **15**, 7657–7665.

22 S. J. Makowski, P. Köstler and W. Schnick, *Chem. - A Eur. J.*, 2012, **18**, 3248–3257.